Progress in Physics of Applied Materials 4 (2024) 135–144

Semnan University

Progress in Physics of Applied Materials

journal homepage: https://ppam.semnan.ac.ir/

GO/Co-MOF/NiMnCu nanocomposite as a possible candidate for the future of the supercapacitor generations

Elham Mazaheri[a], Ali Bahari[a,*], Shahram Ghasemi[b]

[a]*Department of Solid-State Physics, University of Mazandaran, Babolsar, Iran.*
[b]*Faculty of Chemistry, University of Mazandaran, Babolsar, Iran.*

ARTICLE INFO

Article history:
Received: 19 July 2024
Revised: 3 August 2024
Accepted: 3 August 2024

Keywords:
Supercapacitor
Nanostructures
Specific surface area
Metal-Organic Framework (MOF)
Graphene oxide

ABSTRACT

Some issues of the electroactive materials in supercapacitor devices, such as low specific surface area, lower electron/ion transportation, and undesirable conductivity, are threatening the current components of supercapacitor devices. Higher surface adsorption sites and specific surface area in the porous structures could contribute to the enhanced performance. The porous network facilitates higher ion diffusion, higher cyclic retention (which are not discussed in the present work) and improved electrochemical interactions. Improving these factors can cause more occupation sites, more connections between electrode-electrolyte, which means more reaction places for charge storage in the supercapacitor devices. In the present study, we synthesized graphene oxide (*GO*), *Co*-metal-organic framework (*MOF*) / *NiMnCu* nanocomposite on nickel foam (*NF*) (*GO/ CoMOF/ NiMnCu*) samples with solvothermal method. Our findings show that *GO/ CoMOF/ NiMnCu* sample has higher specific surface area, good porosity than their individual components. Thus, *GO/ CoMOF/ NiMnCu* sample has much larger specific capacitance, which can affect the sample structure and improve electrical characteristics, yield to more occupation sites and/or specific surface area, enhancement of the carrier (electrons, ions) transportation in the supercapacitor devices. Therefore, here XRD patterns confirmed metal hydroxides, *Co-MOF* and *GO* formations, and Brunauer-Emmett-Teller *(BET)* results revealed higher pore volume which can cause faster and better transportation of ions, or better performance of sample (*GO/ CoMOF/ NiMnCu*) as a possible material for the next supercapacitor devices.

1. Introduction

In the last decades people around the world have faced the greenhouse problem and requested researchers to find renewable clean energy storage devices [1-3]. Among the so many suggestions for qualified energy storage devices, supercapacitors, as efficient energy storage devices with outstanding advantages, show good potential for this regard [4-5]. The reason could be its high power density, good cyclic stability, fast charging rate (as well as its positive impact cases) in so many electronic chips[5]. This point could be desirable materials with improved surface-engineered redox active materials, fabricating capacitor electrodes with higher carrier mobility, more occupied sites or porosity structures, higher power and energy density, and shorter charge/discharge duration time [5,6]. Therefore, to address the current supercapacitor issues of low conductivity and electrocatalytic activity, several strategies have been proposed.

The first solution route is using the doping metal process, in which, *Co*, *Mn*, *Cu*, and *Ni* can enhance the supercapacitor performance due to their more accessible surface effective sites. The second effective way to solve problems related to charge transport is to merge present material and conduct carbon nanomaterials, including graphene oxide (GO) due to its higher electrical conductivity and its large surface area. Go has 37.17 (m^2 g^{-1}) specific surface area, 20.861

* Corresponding author.
E-mail address: a.bahari@umz.ac.ir

Cite this article as:
Mazaheri, E., Bahari, A. and Ghasemi, S., 2024. GO/Co-MOF/NiMnCu nanocomposite as a possible candidate for the future of the supercapacitor generations. *Progress in Physics of Applied Materials*, 4(2), pp.135-144.DOI: 10.22075/ppam.2024.34800.1109

mean pore size (nm), 0.028 V_{micro} ($cm^3\ g^{-1}$), 0.099 $V_{Meso/macro}$ ($cm^3\ g^{-1}$) and 0.127 total pore volume ($cm^3\ g^{-1}$) [4].

Therefore, metal-organic frameworks (*MOFs*), ZIF-67 (zeolitic imidazolate framework-67) as porous materials or periodic porous material formed by binding ions or clusters of transition metals can be considered as organic ligands via covalent or ionic bonds[1-10]. Therefore, ZHF-67 with *GO*-based and transition metal compounds can be an alternative template to construct multiple 3-dimensional porous structures with desirable characteristics such as good tunable morphology, flexibility of framework, superb flexibility, a large conductive network of nano strings with controllable radius, and good morphology may solve poor electrical conductivity of MOFs. Researchers have tried to synthesize hollow nanostructures using zeolitic imidazolate framework-67 (ZIF-67) as a template, trimetallic nickel-cobalt-manganese hydroxide (*NiCoMn-OH*) polyhedral composites. Hao *et al.,* synthesized ZIF-67 +cotton carbon/Co-Ni-Mn with solvothermal route and reported an outstanding cyclic stability of 91.8 percent -5000 cycles) and 2995.56 F g^{-1} @ 1 A g^{-1}specific capacitance [8]. In another work, Lv *et al.,* showed a hollow core/shell cactus-like *Ni-Co(CO₃)₀.₅(OH) ·0.11H₂0@MnNiCo-OH (Ni-CCH@MnNiCo-OH)* with an not good cyclic stability (about 88 percent -3000 cycles of charge-discharge at 20 mA cm^{-2}) and good specific capacity of 1029.3 C g^{-1} @ 1 A g^{-1} with modifying ZIF-67+ polymetallic co-deposition tactics [7]. Fu *et al.,* announced that their core–shell layered double hydroxide of *NiCeCo* or *CuBr₂@NCC-LDH/ CF* electrode, synthesized with hydrothermal procedure show so good areal capacitance of 5460 mF cm^{-2} @ 2 mA cm^{-2} in a cyclic stability of 88 percent @ 50 mA cm^{-2}[11].

In the present work, we could synthesize *GO/ Co-MOF /NiMnCu* with ZIF-67 using solvothermal route and studied the sample characteristics with using X-ray patterns (XRD), Fourier transform infra-red (FTIR) spectroscopy, Raman spectroscopy, and Brunauer-Emmett-Teller (BET) method (For measuring the amount of physically adsorption/desorption gas process, here nitrogen gas). We could find higher specific surface area (S_{BET}), 1.2 times higher for *GO/Co-MOF/ NiMnCu* with ZIF-67 than that of *Co-MOF/ NiMnCu* with ZIF-67. As reported in [11-20], these results can give us better and desirable electrochemical performance and outstanding cyclic stability, which is a suitable finding for the next supercapacitor generations.

2. Experimental procedure and details

As shown in Table 1, materials used in the present work have suitable purity, bought from Merck Company. In Figure 1, the structure of some materials used in the present work is given.

Fig. (2) shows graphite oxide (*GO*) and *GO/ Co-MOF* synthesize procedures, and Figure 3 also shows the preparation procedure of *NF/ GO/ Co-MOF/ NiMnCu* with using the modified Hummers' route.

Table 1. Materials used in the present synthesize procedure.

Material	% Purity
cobalt (II) nitrate hexahydrate	99
nickel (II) nitrate hexahydrate	99
copper (II) chloride dihydrate	99
N, N-dimethyl formamide (DMF)	99
2-methylimidazole	98
methanol	99.5
manganese (II)-chloride tetrahydrate	99
ethanol	99.7
potassium hydroxide	85
graphite flakes	99
sulfuric acid	98
potassium permanganate	99
H_2O_2	35
hydrochloric acid	37
nickel foam (NF)	89

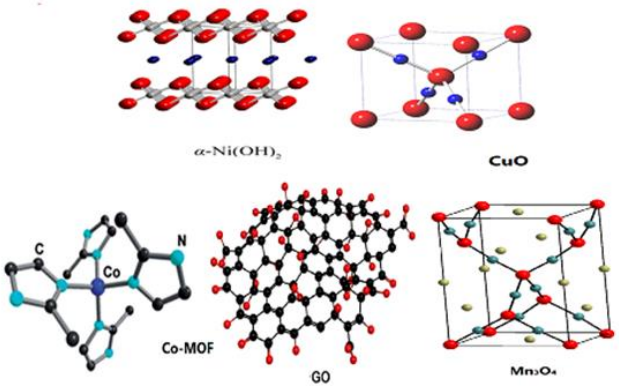

Fig. 1. The structure of a- $Ni(OH)_2$, CuO, Co- MOF, GO, and Mn_3O_4 [5].

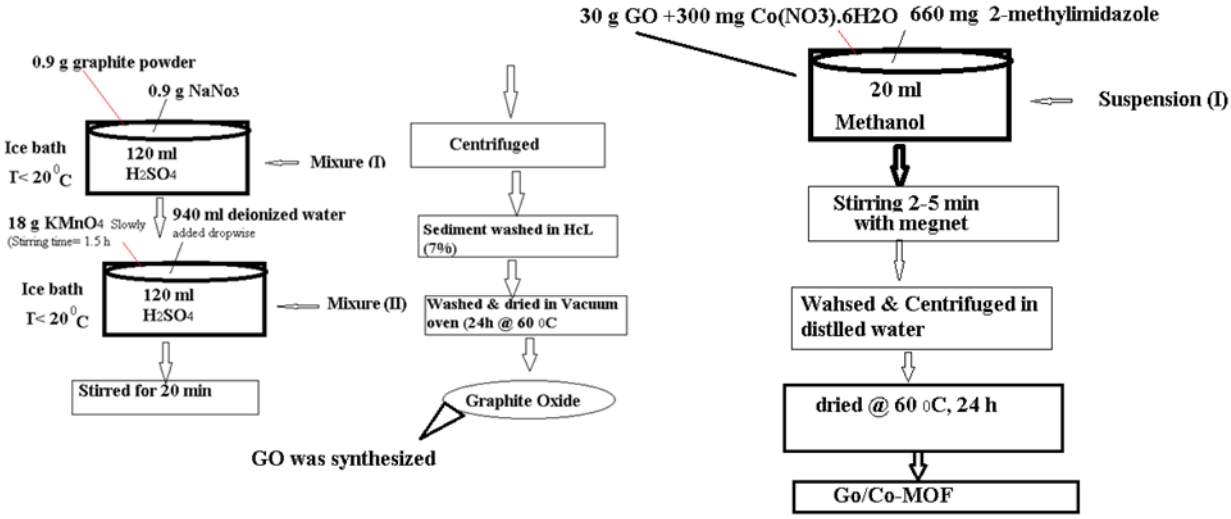

Fig. 2. Preparation procedure of Go and Go/Co-MOF.

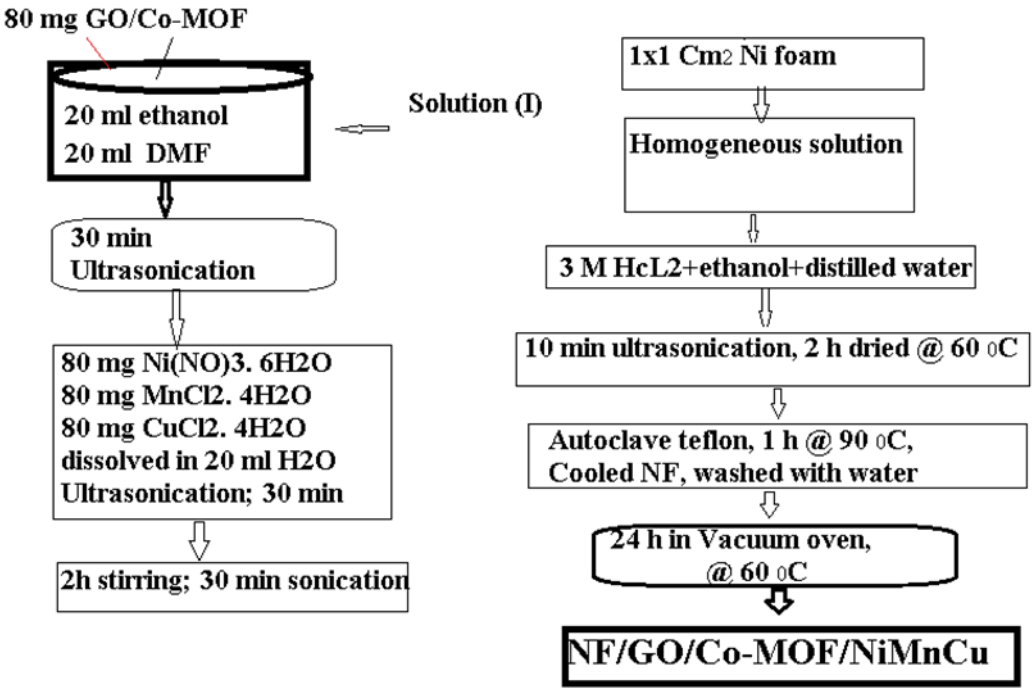

Fig. 3. Preparation procedure of *NF/ GO/ Co-MOF/ NiMnCu.*

3. Results and discussion

3.1. Structural characterization

To investigate the nanostructural properties, porosity, and specific surface area, X-ray diffraction spectroscopy (XRD), Fourier transform infrared (FTIR) spectroscopy, Raman spectroscopy, and Brunauer-Emmett-Teller (BET) method were used. XRD patterns in Figure 4 reveal crystalline structures and crystallite's phases (labelled with Miller index, (hkl)) of dominated peaks (Figure 4-up) in the 5-25° range for *GO* (called here, sample *A*), *Co-MOF* (called here, sample *B*), *GO/ Co-MOF* (called here, sample *C*) , and (Figure 4-down) *Co-MOF/ NiMnCu* (called here, sample *D*), and *GO/Co-MOF/ NiMnCu* (called here, sample *E*). The samples' location and crystallite phases, shown in Figure 4 and Table 2, confirm successful synthesis from graphite flakes [14]. For instance, a dominated peak of sample (*A*) at about 9.4° (001) with the d-spacing of 9.4 Å and checking with [14-16], indicates the formation of Go. Also, it can make broad interlayer distance between consecutive layers. This issue may be due to H_2O- O_2 functional groups and creation of the intercalation in the graphite layers.

The other crystalline planes of sample (*A*) are presented in Table 2; in where another peak (hkl= 003 or 001) at about 7.8°, and d-spacing of 11.2 Å, could be due to the existence of the residual unreacted graphite flake remained in the sample (*A*), which was checked with (CCDC 1603486).

It is clear from Figure (4-up) that the samples (*B, C*) have crystalline structure, in that their dominated peaks appeared at the same location with different intensity (This different intensity of the samples *B* and *C*) could be due to the coverage characteristic of the graphite oxide [10]. As denoted with small circles in this XRD pattern, small peaks indicate not only the successful hybridization of *GO* and *Co-MOF* [12], but also the effect of the interband transition and surface plasmon [21] (which need more details and will be discussed in our future work). But, XRD patterns of the samples (*D*) and (*E*) in Figure (4-down) exhibit a lack of the sample (*B*) characteristic peaks and the distortion of the samples (*D,E*) chemical framework.

In conclusion, we found that Ni, Mn, and Cu salts revealed in XRD pattern of the present samples affect the sample crystallite phases and their sharp peak is changed and yield to new broad peaks, meaning smaller crystallite size. To find the effect of the $Ni(OH)_2$ (with hexagonal structure; CCDC 1637205), $Mn(OH)_2$ (with hexagonal structure; CCDC 1600154), and $Cu(OH)_2$ (with cubic structure; CCDC 1596200) in the present sample; crystallite phases denoted as samples of $Ni(OH)_2$ +0.75 H_2O, Mn_3O_4, and CuO, data given in Table 3 can help us to get more details.

Similar characteristic of samples (*A, E*) (indicated by yellow circles), demonstrated a successful hybridization of *GO* and *Co-MOF/ NiMnCu* [13]. In addition to successful hybridization stated above, *Ni (OH)₂*, *Mn₃O₄*, and *CuO* have also similar crystallite phases, which show similar crystallite phase's behaviors of MOFs.

Apart from XRD discussions, we studied the chemical structures of the present samples by looking at FTIR spectra (the wavenumber range is from 400 to 4000 cm^{-1}). Again, we present FTIR (shown in Figure (5)) wavenumber locations of the chemical bonds for the samples (*A, B, C, E*) in Table 4.

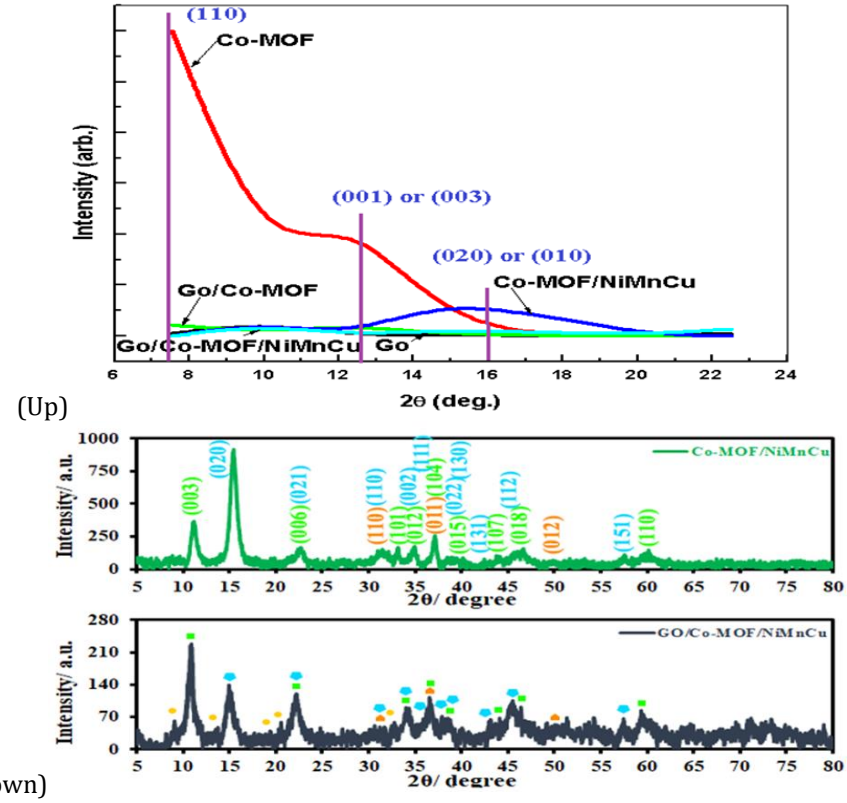

Fig. 4. XRD patterns of samples (*A, B, C*) (up) and samples (*D, E*) (down).

Table 2. Crystallite phases (hkl) and the locations of XRD peaks 2θ (°) for sample (A).

(hkl)	2θ (°)	(hkl)	2θ (°)	(hkl)	2θ (°)	(hkl)	2θ (°)
110	7.5	422	25.9	554	43.6	102	65.2
200	10.4	431	26.9	662	46.9	221	66.3
211	12.8	440	29.8	840	48.1	124	70.4
220	14.8	433	30.7	655	50.0	443	71.4
310	16.5	442	31.8	844	53.2	120	74.3
222	18.1	532	32.6	666	56.7	133	75.8
321	19.6	622	35.1	871	58.2	126	76.3
400	21.0	444	36.8	880	62.1	101	77.0
411	22.3	550	37.7	972	63.8	111	78.2
332	24.6	800	42.7	106	64.3	135	80.0

Table 3. Crystallite phases (hkl) and the locations of XRD peaks 2θ (°) for samples of $Ni(OH)_2$ + 0.75 H_2O, Mn_3O_4, and CuO.

(hkl) ✱ $Ni(OH)_2$ +0.75 H_2O	2θ (°) $Ni(OH)_2$ +0.75 H_2O	(hkl) ■ Mn_3O_4	2θ (°) Mn_3O_4	(hkl) Mn_3O_4	2θ (°) Mn_3O_4	(hkl) ● CuO	2θ (°) CuO
003	11.4	101	18.1	303	53.9	101	24.5
006	22.7	112	28.9	321	54.2	110	32.2
101	33.5	200	31.1	224	56.0	111	35.2
012	34.4	103	32.5	314	58.8	210	38.5
015	38.8	211	36.2	305	60.0	200	44.3
018	46.0	004	38.3	413	64.7	311	48.6
110	60.0	220	42.6	404	70.0	310	53.3
113	61.2	204	50.1	-	-	111	61.3
-	-	105	51.0	-	-	113	75.9

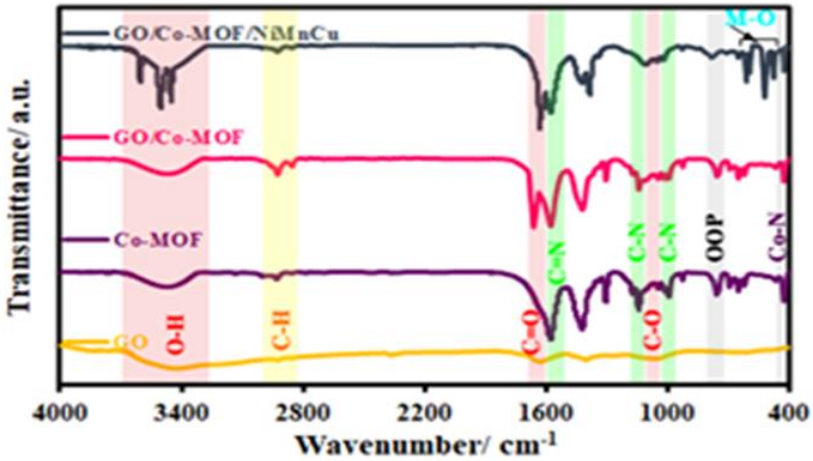

Fig. 5. FTIR spectra of samples (*A, B, C, E*).

Table 4. Chemical bonds and the wavenumber locations of FTIR peaks for samples.

sample	Wavenumber (cm^{-1})	Chemical bond location	Note: it is due to …
A	3427	O-H	different O_2- functional groups
A	1632	C=O	different O_2- functional groups
A	1049	C-O	different O_2- functional groups
B	2830-3010		
B	1580	stretching vibrations of C=N	2-methylimidazole ligands
B	1140, 991	C-N	Bending & stretching vibrations of C-N bond
B	756, 692	bending vibration of the ring in 2-methylimidazole	out-of-plane vibrations [12]
B	424	stretching vibration of Co-N	Co ions + N in 2-methylimidazole, in the sample (B)
Samples (*A-E*)	3500	stretching vibration of O-H	H-bounding between OH groups with interlayer water molecule [14]
Samples (*B-E*)	609-474	stretching vibration of M (Ni, Mn, Cu)-O	metal hydroxides

As shown in Figure 5, FTIR spectra of the samples (*C, E*) with little bit wavenumber changes indicate that these samples have nearly same chemical structure, with different intensities due to different intercalated M (*Ni, Mn, Cu*) in the sample *Co-MOF* during the synthetic procedure. There is same scenario for samples (*A*), (*B*), and (*E*), which shows a series peaks related to both *GO* and *Co-MOF* with

different shapes of the intense and broad band centered at 3500 cm^{-1}, attributed to the O–H stretching vibration of H-bounding between OH groups with interlayer water molecule [14], but also approves formation of different metals (here; *Ni, Mn, Cu*) hydroxides in the sample, as proved this claim in the wavenumber 609-474 cm^{-1} for M–O and M-O-M (M= Mn, Ni, Cu) stretching vibration in synthesized metal hydroxides. Finally, Figure 5 shows that GO and Co-MOF chemical bonds are appeared in the all-present samples.

In parallel to discussion related to XRD and FTIR, Raman spectra of the samples (*A-C, E*), shown in Figure 6, indicate the role of crystallite defects to the nanostructural characteristics of the samples. There are three bands of the sample (*A*): 1- D @ Raman shift;1351cm^{-1}, 2- G@ Raman shift;1603 cm^{-1}, and 3- 2D@ Raman shift; 2913 cm^{-1}). G- and D- band with nearly the same intensity exhibits the formation of the carbons with sp^2 hybridization, whilst D-band is due to distortion from sp^2 hybridization, and/or distortion of graphene basal plane in the synthesize process of oxidation reactions [15, 18]. A small peak at about 600 cm^{-1} in Figure 6 in sample (*B*) disappeared after adding *GO* crystallites and other peaks Co-O and Co-OH bonds because of covering effect of *GO* at lower Raman shift for sample (*C*) formed.

There is another small peak in Figure 6 at Raman shift= 2900 cm^{-1} due to 2D band, which is not due to a defect in sample structure, meaning it does not reveal defects, could originate from a double resonance enhanced two-phonon lateral vibrational process.

Other points that have been emphasized in this study are specific surface area and porosity distribution, which are investigated with the BET technique, and the results of the investigations are shown in Table 5 and Figure 7. BET analysis is one of the methods of measuring and checking surface porosity. Accurate measurement of surface area and cavities is very important in many applications such as catalysts, nanoabsorbents, pharmaceuticals and food industries, as well as in nanostructures such as metal nanoparticles, nanotubes, nanofibers, etc. Among the different methods used to determine the porosity, the BET method is based on gas absorption. The basis of BET analysis is based on measuring the volume of absorption and desorption of nitrogen gas molecules on the surface of the material prepared at constant temperature. In this method, a complete layer of absorbed material molecules is placed on the surface. By knowing the average thickness of a molecule, it is possible to calculate the surface occupied by a molecule and measure the total surface area of the sample based on the amount of absorbed substance. BET analysis was used to determine the active surface areas, average porosity of GO, Co-MOF, GO/Co-MOF, Co-MOF/NiMnCu, and GO/Co-MOF/NiMnCu nanocomposite crystals, and their absorption and desorption diagram are depicted in Table 5 and Figure 7.

In addition, the five curves with apparent hysteresis loops can be classified as type IV hysteresis curves. Surface area and pore size distribution are two key factors for electro-active materials that are used in supercapacitors for electrical storage applications and confirm the interaction between a material and its surroundings. Because by increasing the surface area of the electrode, the number of active sites or in other words the number of sites increases. Therefore, the oxidation and reduction reaction and ion transfer are accelerated. Increasing the specific surface usually creates more contact surface between the electrode and the electrolyte and provides enough reaction spaces to store charges. In addition, the pore size distribution was investigated by Bruner-Emmett-Teller (BET) method. All these samples show a wide size distribution. *Co-MOF, GO/Co-MOF, Co-MOF/ NiMnCu* and *GO/Co-MOF/NiMnCu* nanocomposite, except for GO nanoparticle, their pores are composed of micropores (microporosity) and have micropores with distribution sizes in the range of 2 nm. Figure 7 (*A, B, C, D,* and *E*) demonstrates adsorption and desorption behavior of five prepared materials of nanoparticles *GO, Co-MOF, GO/Co-MOF*, *Co-MOF/ NiMnCu* and nanocomposite *GO/ Co-MOF/NiMnCu*. The *GO* curve shows the IV isotherm with H_3 residue, which represents the mesoporous structure. The *Co-MOF* curve shows the IV isotherm with a small H_2 residual loop, which is a microporous structure with interconnected networks. The residue of *GO/Co-MOF* has been observed at a higher relative pressure ($P/P<0.5$), which indicates a large number of micropores on the surface of *GO/Co-MOF* nanoparticles. The curve of *GO/Co-MOF* and *Co-MOF/NiMnCu* shows isotherm IV with a 4H residual loop, which represents the microporous structure with wide and irregular distribution of particles. In the *Co-MOF/NiMnCu* curve, the desorption curve at ($P/P_0> 0.6$) is almost connected to the absorption curve, which indicates that the opening of the holes is almost open. The *GO/Co-MOF/ NiMnCu* curve shows the IV isotherm with a 3 H residual loop, which indicates the presence of the microporous structure of the prepared sample. The specific surface area of *GO, Co-MOF, GO/Co-MOF, Co-MOF/NiMnCu,* and nanocomposites are 4/345, 1913/6, and 1703/9 m^2g^{-1}, respectively. It is 452.378 and 452.55 m^2g^{-1}, which was calculated by BET method. All these samples have a distinct surface area and this is due to their different and unique morphologies. The large surface area of *Co-MOF* is due to its organometallic framework structure. A significant increase in surface area can be seen with the formation of *GO/Co-MOF/NiMnCu*, therefore, among all these particles (except *Co-MOF* and *GO/Co-MOF*), the specific surface area is wider. In fact, the large surface area of the active substance leads to the creation of many active sites for the Faraday process. The calculated particle size distribution is very high, which indicates the presence of a large number of pores between 0 and 2 nm. Therefore, the structure of all materials is microporous, which can be seen in Figure (4-6 A, B, C, D, and E). The specific volume of the porous structures of *GO, Co-MOF, GO/Co-MOF, Co-MOF/NiMnCu,* and nanocomposite *GO/Co-MOF/NiMnCu* are 0.0071, 0.6642, and 0.4935 ($cm^3 g^{-1}$), respectively. 0.716 and 0.99198 ($cm^3 g^{-1}$).

These issues are very important in the investigation of electrical storage device, here electroactive materials in supercapacitors. As reported by some researchers [13-20], it can lead to a sample with more occupation sites (reaction places) for charge storage and a more specific surface area (or more interface between electrode-electrolyte).

In this regard, we used nitrogen gas to the sample (*A*) structure and measured N_2 gas adsorption/desorption,

appeared as IV isotherms with hysteresis loops and with a wide size distribution, show microspores structure. From Table (5), S_{BET} of sample (*E*) (= 452.55 $m^2 g^{-1}$), is about 1.2 times of S_{BET} for sample (*D*) (sample (*E*) without *GO*) (which is equal to 378.17 $m^2 g^{-1}$). Therefore, this finding shows that GO could affect the sample structure and give better S_{BET} or more occupied sites and porous structures. Higher occupied sites and/or porous structures can improve both electrolyte reservoir and volume variation of the Faradic reactions. In other words, with higher S_{BET} pore volume, and accessible sites, better electrolyte ion transfer can occur, as discussed in detail in Ref. [16].

From Table 5, sample *B* with a higher specific surface area (= 1913.6 $m^2 g^{-1}$), sample *C* with higher mean pore diameter (= 1.6265 nm), and sample *E* with a higher total pore volume (= 0.99198 $cm^3 g^{-1}$), not only show structure without aggregated occupied sites, but also indicate superior performance of the present nanocomposite material.

Electrochemical energy storage tests

The excellent supercapacitor performance with superior Coulombic efficiency of 98.4% and retention of 73% capacitance after 5000 cycles shows this material as a potential candidate for supercapacitors. A comparative electrochemical study of the present sample was performed in a three-electrode system, the electrochemical performance was more related to their physical and chemical properties [7-10]. This unique structure could increase the electrochemical active site of the composite and enhance the Faraday oxidation-reduction reaction and increase its electrochemical properties.

Incorporation of GO into Co-MOF/NiMnCu increased the conductivity and electrochemical performance. The electrochemical properties of this composite were evaluated in (M5) KOH solution. The produced composite (1162 Farads/g) showed higher specific capacitance than Co-MOF/NiMnCu without GO (978 Farads/g). This result indicated that the fabricated GO/Co-MOF/NiMnCu composite may be used as an electrode material for supercapacitor applications.

In Figure 8, CV curve or cyclic voltammetry diagram of GO, Co-MOF, GO/Co-MOF, Co-MOF/ NiMnCu, and GO/Co-MOF/NiMnCu nanocomposite materials in the voltage window -0.1 to 0.7 V and at a scanning speed of 5 mV/s is shown. It is clear that the enclosed area in the CV diagram shows the electrochemical performance of the synthesized samples. As the level of these curves rises, so does the specific capacity.

As we know, if the CV curve of a material is almost rectangular, it means that the energy storage in that material is mostly in the form of a double-layer mechanism.

But according to the Figure 8 in the 5 mV/s scanning, dominated oxidation-reduction peaks can be seen. The desired electrode materials have quasi-capacitive behavior. This is due to the existence of functional groups on the surface of GO and nitrogen bonds that enter redox reactions. This result can be confirmed by, noting to two oxidation-reduction peaks in the Co-MOF curve in the potential range of 0.3 to 0.4 V. This behavior is due to chemical reactions at the electrode-electrolyte boundary. These characteristics of faradaic pseudo-capacitance of the electrode lead to the deviation of the CV curve from the rectangular state [13], whilst this behavior is not appeared in GO/Co-MOF curve, therefore Co-MOF, Co-MOF/NiMnCu, and GO/Co-MOF/NiMnCu nanocomposite have better redox performance. The surface area inserted in this diagram is increased compared to Co-MOF/NiMnCu, hence the specific capacity increases, and this is due to the presence of GO and the strong Π-Π interaction between Co-MOF/NiMnCu and GO [10-15]. When GO is part of the GO/Co-MOF/NiMnCu structure, it stops the synthesized nanoparticles from slowly building up. This makes the specific capacity higher.

In addition, GO in the Co-MOF/NiMnCu mix also creates a continuous network of conductors that makes it easier for ions to move and for the redox process to happen [14].

As a result, the surface contact between the electrolyte and GO/Co-MOF/NiMnCu increases, while the charge transfer resistance decreases.

Therefore, it plays an effective role in improving the electrochemical performance of the GO/Co-MOF/NiMnCu electrode.

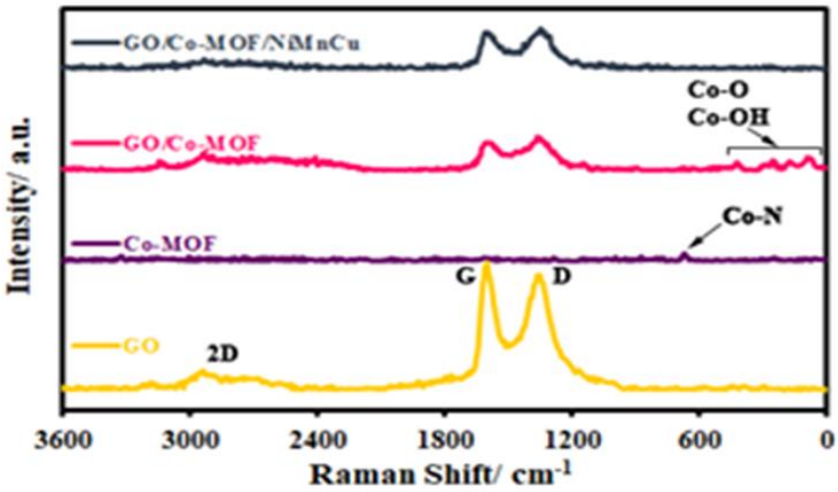

Fig. 6. Raman spectra of samples.

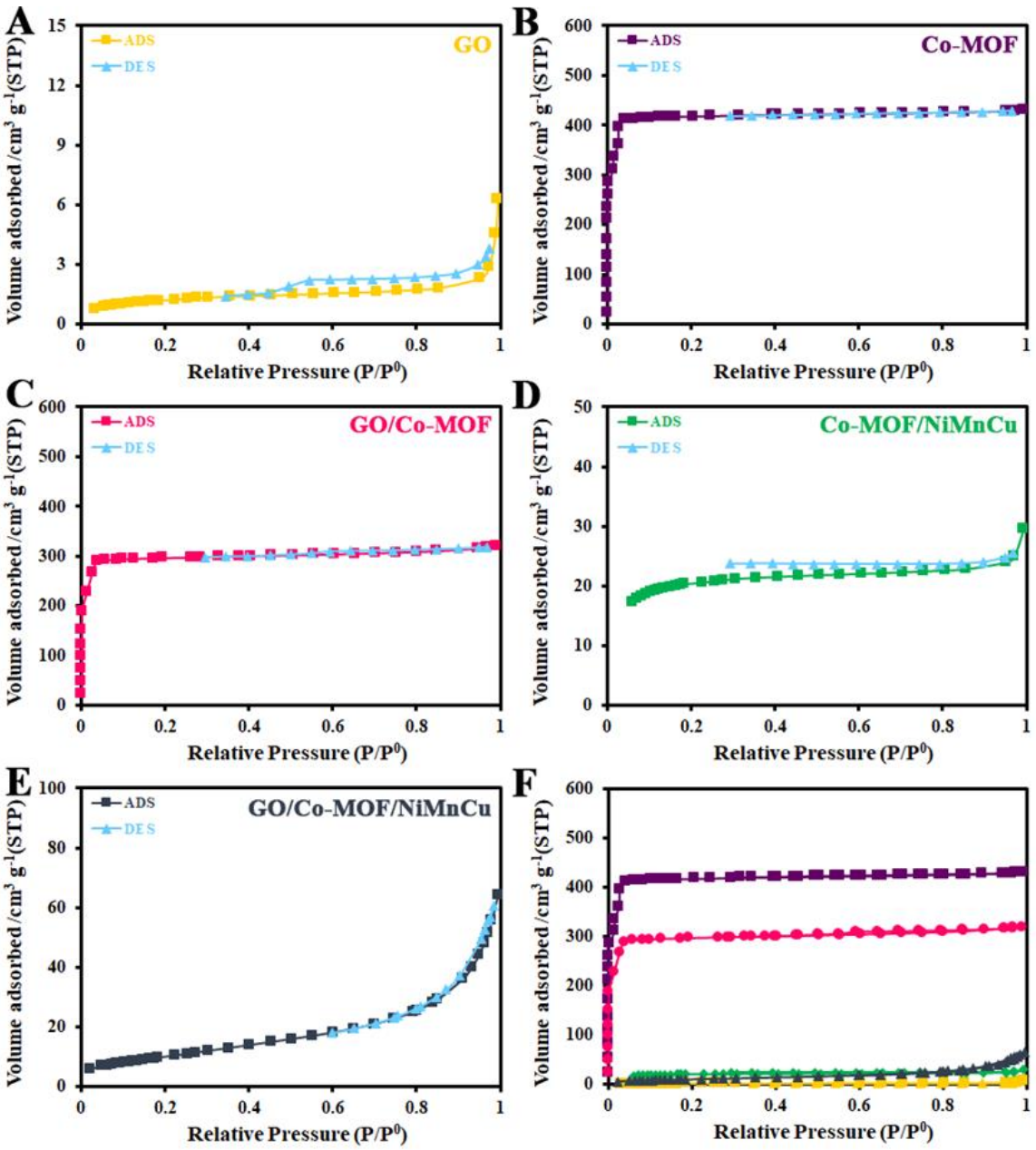

Fig. 7. N_2 adsorption-desorption isotherms of the samples and (*F*) all in one.

Table 5. Results of porosity and effective surface area measured by BET.

BET parameter	GO	Co-MOF	GO/Co-MOF	Co-MOF/NiMnCu	GO/Co-MOF/NiMnCu
Specific area (m^2g^{-1})	4.345	**1913.6**	1703.9	378.17	452.55
Total pore volume ($cm^3\ g^{-1}$)	0.0071	0.6642	0.4935	0. 716	**0. 99198**
Mean pore diameter (nm)	6.48	1.5593	**1.6265**	1.103	1.0003

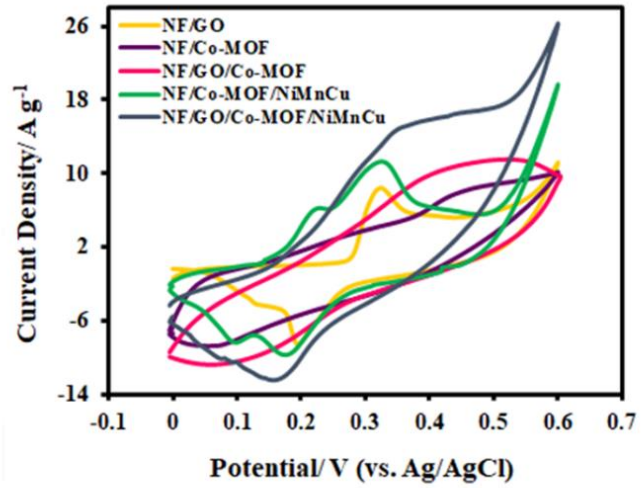

Fig. 8. Cyclic voltammetry diagram of all samples in the voltage window of -0.1 to 0.7 V and at a scanning speed of 5 mV/s.

4. Conclusion

In the present work, we could synthesize GO/Co-MOF/NiMnCu (sample E) nanocomposite with hydrothermal route and analyze their nanostructural, porosity, and specific surface area with some relevant techniques (XRD, FTIR, Raman spectroscopy, and BET or N_2 adsorption-desorption process) for getting more sites and/or better carrier transportation. The obtained results from XRD patterns confirmed metal hydroxides, Co-MOF, and GO formations. BET results revealed higher pore volume, which can cause faster and better transportation of ions, or better performance of sample E as a possible material for the next supercapacitor devices.

Acknowledgements

This research received no external funding.

Conflicts of Interest

The author declares that there is no conflict of interest regarding the publication of this article.

References

[1] Yue, L., Chen, L., Wang, X., Lu, D., Zhou, W., Shen, D., Yang, Q., Xiao, S. and Li, Y., 2023. Ni/Co-MOF@ aminated MXene hierarchical electrodes for high-stability supercapacitors. Chemical Engineering Journal, 451, p.138687.

[2] Salmani, H. and Bahari, A., 2019. GO/C_2S gate dielectric material for nanoscale devices obtained via Pechini method. *Surface Engineering and Applied Electrochemistry*, *55*, pp.379-389.

[3] Kenari, K.H., Bahari, A. and Lashkenari, M.S., 2023. Widely improved supercapacitance properties of zirconium-cobalt ferrite nanoparticles by N-doped graphene oxide as an electrode in supercapacitor. *Journal of Energy Storage*, *74*, p.109274.

[4] Moghaddam, M.S., Bahari, A. and Litkohi, H.R., 2023. Using the synergistic effects of MoS_2/rGO and bimetallic hybrids as a high-performance nanoelectrocatalyst for oxygen reduction reaction. *International Journal of Hydrogen Energy*, *48*(85), pp.33139-33154.

[5] Acharya, D., Pathak, I., Dahal, B., Lohani, P.C., Bhattarai, R.M., Muthurasu, A., Kim, T., Ko, T.H., Chhetri, K. and Kim, H.Y., 2023. Immoderate nanoarchitectures of bimetallic MOF derived Ni–Fe–O/NPC on porous carbon nanofibers as freestanding electrode for asymmetric supercapacitors. *Carbon*, *201*, pp.12-23.

[6] Liu, R., Zhou, A., Zhang, X., Mu, J., Che, H., Wang, Y., Wang, T.T., Zhang, Z. and Kou, Z., 2021. Fundamentals, advances and challenges of transition metal compounds-based supercapacitors. *Chemical Engineering Journal*, *412*, p.128611.

[7] Lv, H., Zhang, X., Wang, F., Lv, G., Yu, T., Lv, M., Wang, J., Zhai, Y. and Hu, J., 2020. ZIF-67-assisted construction of hollow core/shell cactus-like MnNiCo trimetal electrodes and Co, N dual-doped carbon electrodes for high-performance hybrid supercapacitors. *Journal of Materials Chemistry A*, *8*(28), pp.14287-14298.

[8] Hao, C., Wang, X., Wu, X., Guo, Y., Zhu, L. and Wang, X., 2022. Composite material CCO/Co-Ni-Mn LDH made from sacrifice template CCO/ZIF-67 for high-performance supercapacitor. *Applied Surface Science*, *572*, p.151373.

[9] Trivedi, H., Verma, K.D., Sinha, P. and Kar, K.K., 2021. Current collector material selection for supercapacitors. *Handbook of Nanocomposite Supercapacitor Materials III: Selection*, pp.271-311.

[10] Li, L., Wu, Z., Yuan, S. and Zhang, X.B., 2014. Advances and challenges for flexible energy storage and conversion devices and systems. *Energy & Environmental Science*, *7*(7), pp.2101-2122.

[11] Fu, H., Zhang, A., Jin, F., Guo, H. and Liu, J., 2022. Ternary NiCeCo-layered double hydroxides grown on $CuBr_2$@ ZIF-67 nanowire arrays for high-performance supercapacitors. *ACS Applied Materials & Interfaces*, *14*(14), pp.16165-16177.

[12] Ediati, R., Elfianuar, P., Santoso, E., Oktavia Sulistiono, D. and Nadjib, M., 2019. Synthesis of MCM-41/ZIF-67 composite for enhanced adsorptive removal of methyl orange in aqueous solution. *Mesoporous Materials-Properties and Applications*, pp.1-14.

[13] Zhang, L., Cai, P., Wei, Z., Liu, T., Yu, J., Al-Ghamdi, A.A. and Wageh, S., 2021. Synthesis of reduced graphene oxide supported nickel-cobalt-layered double hydroxide nanosheets for supercapacitors. *Journal of Colloid and Interface Science*, *588*, pp.637-645.

[14] Ghadimi, A.M., Ghasemi, S., Omrani, A. and Mousavi, F., 2023. Nickel cobalt LDH/graphene film on nickel-foam-supported ternary transition metal oxides for supercapacitor applications. *Energy & Fuels*, *37*(4), pp.3121-3133.

[15] Hu, G., Zhang, W., Chen, Y., Xu, C., Liu, R. and Han, Z., 2020. Removal of boron from water by GO/ZIF-67 hybrid material adsorption. *Environmental Science and Pollution Research*, *27*, pp.28396-28407.

[16] Le, K., Wang, Z., Wang, F., Wang, Q., Shao, Q., Murugadoss, V., Wu, S., Liu, W., Liu, J., Gao, Q. and Guo, Z., 2019. Sandwich-like NiCo layered double hydroxide/reduced graphene oxide nanocomposite cathodes for high energy density asymmetric supercapacitors. *Dalton Transactions*, *48*(16), pp.5193-5202.

[17] Li, M., Cheng, J.P., Liu, F. and Zhang, X.B., 2015. 3D-architectured nickel–cobalt–manganese layered double hydroxide/reduced graphene oxide composite for high-performance supercapacitor. *Chemical Physics Letters*, *640*, pp.5-10.

[18] Najjar, R., Awad, R. and Abdel-Gaber, A.M., 2019. Physical properties of Mn_2O_3 nanoparticles synthesized by Co-precipitation method at different pH values. *Journal of Superconductivity and Novel Magnetism*, *32*, pp.885-892.

[19] Ghasemi, S., Hosseini, S.R. and Mousavi, F., 2017. Electrophoretic deposition of graphene nanosheets: A suitable method for fabrication of silver-graphene counter electrode for dye-sensitized solar cell. *Colloids and Surfaces A: Physicochemical and Engineering Aspects*, *520*, pp.477-487.

[20] Li, F., Sun, Z., Jiang, H., Ma, Z., Wang, Q. and Qu, F., 2020. Ion-exchange synthesis of ternary FeCoNi-layered double hydroxide nanocage toward enhanced oxygen evolution reaction and supercapacitor. *Energy & Fuels*, *34*(9), pp.11628-11636.

[21] Shajari, D., Bahari, A., Gill, P. and Mohseni, M., 2017. Synthesis and tuning of gold nanorods with surface plasmon resonance. *Optical Materials*, *64*, pp.376-383.